GHz Low-Loss Acoustic RF Couplers in Lithium Niobate Thin Film

Ruochen Lu, *Member, IEEE*, Yansong Yang, *Member, IEEE*, Ming-Huang Li, *Member, IEEE*, and Songbin Gong, *Senior Member, IEEE*

***Abstract*— We present the first group of GHz low-loss acoustic radio frequency (RF) couplers using the fundamental symmetric (S0) mode in X-cut lithium niobate thin films. The demonstrated multistrip couplers (MSCs) significantly surpass the insertion loss (IL) and the operating frequency of the previous works in more compact structures, thanks to the large electromechanical coupling and low loss of S0 in lithium niobate. The design space of S0 MSCs is first explored. Devices with different coupling factors are fabricated using different numbers of strips. Based on the S0 testbed with an IL of 4.5 dB at 1 GHz, the hybrid coupler shows an IL of 7.5 dB, while the track changer shows an IL of 5.1 dB, over a 3-dB fractional bandwidth of 8%. Couplers at different frequencies (between 0.75 and 1.55 GHz) are also investigated. Upon further optimizations, the S0 MSC platform can potentially enable low-loss wideband signal processing functions toward an RF acoustic component kit.**

***Index Terms*— Acoustic delay line (ADL), directional coupler, lithium niobate, microelectromechanical systems, multistrip coupler (MSC), piezoelectricity, S0 mode.**

I. Introduction

RADIO frequency (RF) and microwave frequency signal processing has been an active area of research ever since Marconi's first transmission over the Atlantic [1]. Numerous early applications, including wireless communication [2] and radar [3], fueled the development and maturing of RF and microwave components that eventually led to the emergence of portable or mobile phones in the late 1970s [4]. From then on, driven by the explosive demand for more data, portable wireless systems have gone through multiple generations and have advanced to an unprecedented multiplexity seen today [5]. More parallel RF bands and paths are added in the same form factor, bringing along more components and tighter integration [6]. Designing portable systems faces the new challenge of reducing component size while still operating at RF where the path attenuation is low and fading is readily manageable, especially at the ultrahigh frequency (UHF) range, where the performance of conventional discrete elements starts to degrade while the electromagnetic (EM) waveguides are still bulky (scale with wavelength at RF, typical $\sim$10 s $\cdot$ cm) [7]. Hence, radical size reduction of several orders of magnitude can only be attained by resorting to a physical domain other than EM, namely, acoustic waves with 4–5 orders of smaller wavelengths [8]. A successful example of adopting such a philosophy is bulk and surface acoustic wave devices whose rise in popularity was indeed ushered by the ubiquity of mobile phones [9], [10].

As the advances continue and multiplexity increases in future generation wireless [11], one cannot help to hypothesize that the same design philosophy of exploiting acoustics, if diffused into the implementation of other RF front components, may further reduce system size and enhance capability. In fact, attempts of such nature have been made in the past for couplers [12]–[18] and correlators [19], [20], and also more recently for delay lines [21]–[25], oscillators [26], [27], amplifier [28]–[31], impedance matching networks [32]–[35], circulators [36]–[38], and antennas [39]–[41]. Some of these demonstrations have already outperformed the state-of-the-art, while others have shown the potential to do so. Further refinements in materials [42], design [43], and fabrication [44] may put an RF front-end synthesized either purely or predominantly from an RF acoustic component kit on the horizon. As exciting as it sounds now, past developments often battled the challenge of accessing the acoustics over a sufficiently wide bandwidth and subsequently producing application-worthy performance [45]. Fundamentally, this was limited by the lack of high electromechanical coupling (k^2) [46]. In other words, electrical signals could not be converted to the acoustic domain without high insertion loss (IL) or narrow fractional bandwidth (FBW), which unfortunately dwarfed the size benefit harnessed from acoustics [45].

Fortunately, material and fabrication have advanced in the past four decades to the point that such a limitation is now significantly relaxed, particularly with the exploitation of thin-film lithium niobate ($LiNbO_3$). Recently, RF acoustic devices have been demonstrated in thin-film $LiNbO_3$ with simultaneously high k^2 (up to 40%) and low loss for different acoustic modes, including fundamental symmetric (S0) mode [47]–[49], fundamental shear-horizontal (SH0) mode [50]–[52], and first-order antisymmetric (A1) mode [24], [53]–[55]. Particularly, low-loss and wideband acoustic delay lines (ADLs) [56], where RF signals are

Manuscript received October 25, 2019; accepted January 30, 2020. Date of publication February 3, 2020; date of current version June 29, 2020. This work was supported by the DARPA Microsystems Technology Office (MTO) Near Zero Power RF and Sensor Operations (N-ZERO) project Program. *(Corresponding author: Ruochen Lu.)*

Ruochen Lu, Yansong Yang, and Songbin Gong are with the Department of Electrical and Computing Engineering, University of Illinois at Urbana–Champaign, Urbana, IL 61801 USA (e-mail: rlu10@illinois.edu).

Ming-Huang Li is with the Department of Power Mechanical Engineering, National Tsing Hua University, Hsinchu, Taiwan.

Digital Object Identifier 10.1109/TUFFC.2020.2971196

converted into traveling acoustic waves over large FBW [21], promise miniature passive components based on the principle of waveguiding. The aforementioned bottleneck of accessing the benefits in acoustics could be overcome now with thin-film $LiNbO_3$, subsequently leading to low-loss wide-band microwave functions in miniature form factors.

Among different applications, RF couplers are an essential type of multiport RF components [57]–[59] for signal sampling, isolation, generation, and phase shifting [7]. Conventionally, RF couplers are based on EM wave interference in coupled transmission lines [57], [58], waveguides [59], or discrete elements [60], of which the sizes are substantial for portable systems. The established acoustic counterparts for EM couplers, namely SAW-based multistrip couplers (MSCs) that employ patterned metallic strips on piezoelectric substrates [61], provide more design flexibilities [12], [13], [62] and drastically smaller sizes. However, three bottlenecks hinder the applications of SAW MSCs. First, the achievable IL versus FBW design space is limited by the moderate k^2. Second, SAW MSCs require a large number of strips that span over more than 50 wavelengths [12] to implement hybrid couplers due to insufficient k^2. Third, the slow phase velocity (v_p) of SAW restricts MSCs from operation beyond GHz unless sub-500-nm electrodes are adopted at the expense of reduced power handling and linearity. On the contrary, S0 in thin-film $LiNbO_3$ is likely to provide the performance breakthrough, thanks to the demonstrated large k^2, low loss, and fast v_p in the X-cut $LiNbO_3$ [49].

This work aims to demonstrate acoustic directional couplers on the S0 acoustic platform. The fabricated S0 MSCs feature significantly lower IL and higher operating frequency in a more compact structure compared to SAW counterparts. Devices with different coupling factors (20–3 dB) are built using different numbers of strips. Based on the S0 testbed with an IL of 4.5 dB at 1 GHz, the hybrid coupler shows an IL of 7.5 dB, while the track changer (i.e., fully transferring signals to the coupled port) shows an IL of 5.1 dB and a 3-dB FBW of 8%. Couplers at different frequencies (between 0.75 and 1.55 GHz) are also investigated.

This article is organized as follows. Section II provides a general discussion on the design of S0 MSCs, focusing on multistrip designs and S0 ADL testbed designs. Section III presents the fabricated S0 MSCs on $LiNbO_3$ thin films. Section V presents the measured results. The achieved performance is analyzed for further improvement. Finally, the conclusion is stated in Section VI.

II. S0 Mode MSC Design

A. S0 MSC Overview

The schematic of a typical S0 MSC is shown in Fig. 1. The MSC is a four-port device consisting of four sets of piezoelectric transducers on the ends of the suspended thin film and a group of metallic strips in the middle of the structure. The piezoelectric transducers are done with 100-nm-thick aluminum interdigitated transducers (IDTs). A suspended 800-nm-thick X-cut $LiNbO_3$ film acts as an acoustic waveguide and a foundational structure of the device.

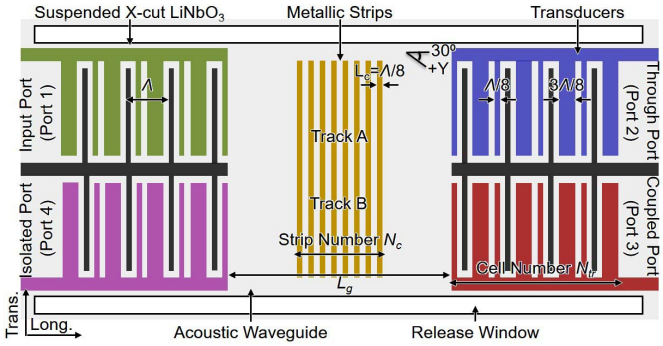

Fig. 1. Mock-up of an S0 MSC on a suspended X-cut $LiNbO_3$ thin film.

The acoustic waveguide is defined by the release windows at the transverse ends. The metallic strips in the middle are done with the same metal layer that defines the IDT. The film stack is chosen for achieving the low-loss and wideband performance at 1 GHz [49]. The device is orientated at 30° to the Y-axis for harnessing the high electromechanical coupling k^2 for S0, and near-zero power flow angle (PFA). More details on S0 acoustic waves in a single-crystal $LiNbO_3$ thin film can be found in previous works [47], [49], [56].

Two pairs of single-phase unidirectional transducers (SPUDTs) are placed on each end. The electrodes in the transducers are alternatingly connected to signals (green IDTs for Port 1, blue for Port 2, red for Port 3, and purple for Port 4) and ground (black IDTs, shared by ports on the same end). Similar terminology for EM couplers is applied here. Upon the designation of the input port (Port 1), the isolated port is the one on the same end of the suspended film (Port 4). The through port (Port 2) faces the input port across the acoustic waveguide, while the coupled port (Port 4) is on the opposite end of the isolated port. Each SPUDT is composed of N_{tr} pairs of cascaded transducer unit cells that each has a width of Λ. Each unit cell includes a pair of transduction electrodes ($\Lambda/8$ wide) and one grounded distributed acoustic reflector ($3\Lambda/8$ wide). The asymmetrical arrangement of the transduction electrodes and the embedded reflectors [45] leads to constructive interference of acoustic waves launched toward device output and destructive interference in the opposite direction. With a sufficient number of cascaded transducer cells, the backward wave propagation is mostly canceled, thus achieving the unidirectionality. By placing input and output SPUDTs facing toward each other, the 6-dB bidirectional IL can be mostly eliminated [45], [49].

Metallic strips (multistrips) are placed in the middle between the input and output ports. The length of each strip is L_c, and the spacing between strips is also chosen as L_c in this work. In operation, the acoustic waves launched from the input port travel across the strips in the upper half of the waveguide (Track A), alternating potential differences are formed between adjacent strips due to piezoelectricity [61]. Such potential differences between electrodes transfer part of the energy to the lower half of the waveguide (Track B), generating acoustic waves traveling toward both the coupled port and the isolated port. As waves propagate across different strips in Track A, the waves generated toward the coupled port

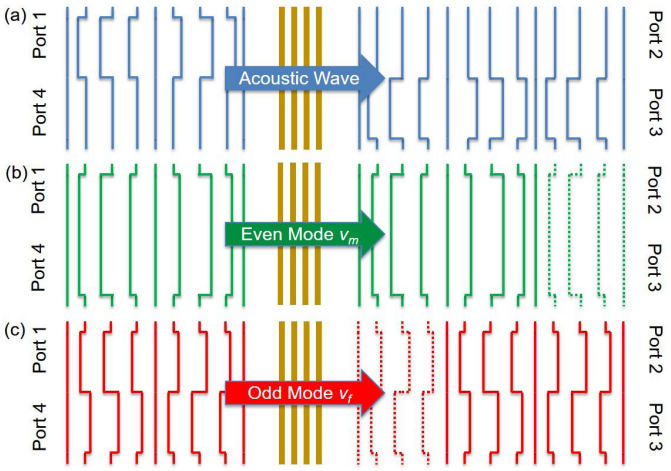

Fig. 2. (a) Input and output acoustic fields decomposed into the (b) even mode and (c) odd mode for an MSC coupling all energy from Port 1 to Port 3. For the even mode and odd mode illustration, the solid lines represent the same period of waves after traversing the multistrips, while the dashed lines denote the period either before or after the one denoted by the solid lines.

build up in Track B, while the waves toward the isolated port cancel out [7]. Therefore, part of the input power is sent into the coupled port, while the remainder still flows to the through port. The device is essentially the acoustic implementation of an EM coupler.

Two factors determine the coupling (S_{31}) of an MSC. First, k^2 of the piezoelectric platform determines the amount of power coupled with a single pair of strips. Second, the number of strips (N_c) determines the total coupling of the MSC.

B. MSC Theory

The performance of multistrips can be quantitatively investigated using the coupled-mode theory [7], [13]. For a perfectly symmetrical structure (see Fig. 2), we first assume that the acoustic waves only propagate along the longitudinal direction. For the case where acoustic waves are launched from Port 1 [see Fig. 2(a)], one can decompose the incident wave into the even mode [see Fig. 2(b)] and the odd mode [see Fig. 2(c)]. The phase of the acoustic wave at each position is plotted, following the sinusoidal function with respect to the longitudinal position. The even mode has in-phase fields in Tracks A and B, while the odd mode has fields 180° out-of-phase between Tracks A and B. Therefore, the input is decomposed as

$$a_1 = (a_{1e} + a_{1o})/2 \tag{1}$$
$$a_4 = (a_{1e} - a_{1o})/2 \tag{2}$$

where a_1 and a_4 are the incident wave amplitudes at Port 1 and Port 4, while a_{1e} and a_{1o} are the even and odd mode incident wave amplitudes at Port 1, with the same value as a_1 before the decomposition. For the even mode, the charge generated in the strips caused by acoustic waves in Track A and B is identical. Therefore, the tracks are decoupled. The even mode propagates at the stiffened velocity v_f across the waveguide section without strips, while at the unstiffened velocity v_m across the waveguide section with strips [46]. The difference between v_f and v_m is proportional to the electromechanical coupling (k^2) of the platform by [63], [64]

$$k^2 = v_f^2/v_m^2 - 1. \tag{3}$$

On the contrary, for the odd mode, the charge generated in both tracks has opposite signs and, thus, cancels out, assuming strips of perfect conductivity [13]. The odd mode travels across the section with multistrips at the stiffened velocity v_f. The output wave amplitudes at Ports 2 and 3 are

$$b_2 = (a_{1e} \cdot e^{-j\omega\delta} \cdot e^{-j\theta_c} + a_{1o} \cdot e^{-j\omega\delta})/2 \tag{4}$$
$$b_3 = (a_{1e} \cdot e^{-j\omega\delta} \cdot e^{-j\theta_c} - a_{1o} \cdot e^{-j\omega\delta})/2 \tag{5}$$
$$\theta_c = \omega \cdot N_c \cdot L_c \cdot (1/v_m - 1/v_f) \approx \pi \cdot k^2 \cdot N_c \cdot L_c/\Lambda \tag{6}$$

where b_2 and b_3 are the output wave amplitudes of Port 2 and Port 3, ω is the angular frequency, δ is the delay for the odd mode to propagate across the strips, θ_c is the phase difference between the even mode propagation and odd mode propagation across the multistrip region with a total length of $N_c \cdot L_c$, and $\Lambda$is the cell length of the SPUDT. Equation (6) indicates that the phase difference is proportional to k^2 and the number of Λ across the strips. From (4) to (6), the S-parameters can be obtained as

$$N_T = \Lambda/(k^2 \cdot L_c) \tag{7}$$
$$|S_{21}| = |b_2|/|a_1| = |\cos(\theta_c/2)| \approx |\cos(\pi N_c/2N_T)| \tag{8}$$
$$|S_{31}| = |b_3|/|a_1| = |\sin(\theta_c/2)| \approx |\sin(\pi N_c/2N_T)| \tag{9}$$
$$\text{phase}_{\text{diff}} = \frac{\pi}{2} \cdot \Sigma \left[2H\left(\frac{N_c}{2N_T} - \frac{2n-1}{2}\right) - H\left(\frac{N_c}{2N_T} - n\right)\right] \tag{10}$$

where N_T is the approximated number of strips required for fully transferring energy from Tracks A to B, n is an integer number, and $H()$ is the Heaviside function with $H(0)$ defined as 1. The amplitude of the transmission is periodic regarding N_c, with a cycle of $2N_T$. The device for full-energy transfer between tracks is also called a track changer [13] and is illustrated in Fig. 2. The even and odd mode waves propagate across the multistrips with different delays, introducing a 180° phase difference. This phase difference is also reflected in Fig. 2 as the wavefronts (the rightest solid green and red lines) are offset by half a period. Such a phase shift causes destructive interference in Track A and constructive interference in Track B, thus transferring waves from Port 1 to Port 3 [see Fig. 2(a)].

The relation between N_T and k^2 is plotted in Fig. 3(a) for $L_c = \Lambda/8$. For acoustic modes with low electromechanical coupling ($k^2 < 5\%$), hundreds of strips are needed for fully coupling energy from Track A to Track B. A larger k^2 can significantly reduce N_T and, thus, lead to a more compact structure.

The amplitudes of S_{21} and S_{31} with different N_c are plotted in Fig. 3(b) for k^2 of 40.4% and L_c of $\Lambda/8$. The value of k^2 is the electromechanical coupling of S0, which will be discussed in Section II-C. A larger portion of acoustic power is transferred to the coupled port for an MSC with more strips on the same piezoelectric platform. Full coupling is achieved when N_c is 23.6, close to the calculated N_T of 19.8, and the

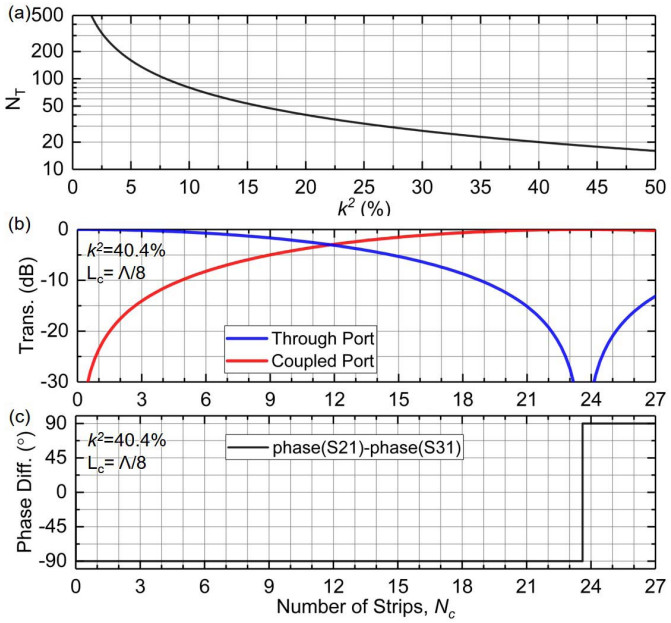

Fig. 3. (a) N_T as a function of k^2. (b) Transmission at the through port and coupled port. (b) Phase difference as a function of N_c, for k^2 of 40.4% and L_c of $\Lambda/8$.

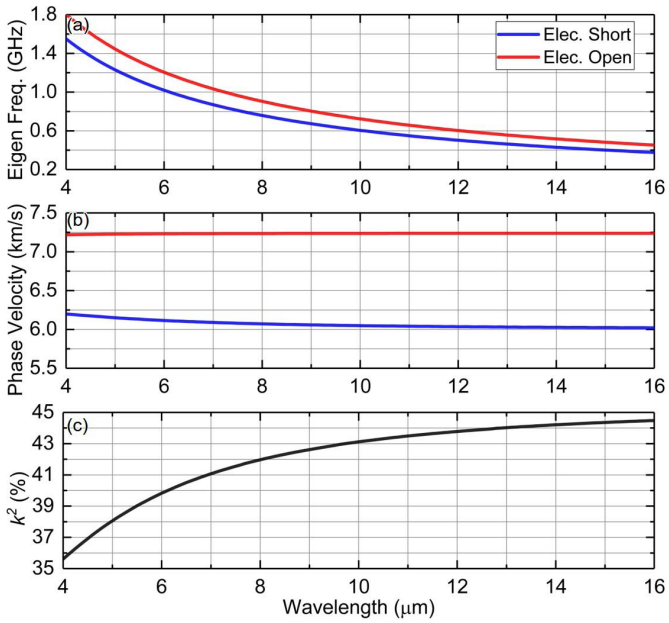

Fig. 4. Simulated characteristics of S0 at different wavelengths in a 0.8-μm-thick X-cut $LiNbO_3$ thin film. (a) Eigen frequency. (b) v_p, with electrically open and short boundary conditions. (c) k^2.

difference is caused by the approximation in (6). Therefore, one can design couplers with different coupling by simply changing N_c. The noninteger values of N_T and N_c mean that full coupling cannot be physically implemented with the given L_c. However, due to the sinusoidal properties of the coupling functions, the coupling provided by the adjacent integer numbers is similar. Besides, one can also fine-tune L_c to achieve an integer number of strips. The phase difference between the through port and the coupled port is 90° [see Fig. 3(c)]. The coupled port leads in phase before reaching full coupling, while the through port leads in phase after the coupling is maximum and before the coupling diminishes to zero again with an increasing number of strips. Phase difference other than 90° can also be achieved by offsetting multistrips in Tracks A and B, which will be discussed in Section II-F.

Note that the results in this section are based on an ideal MSC. The reflections introduced by MSC will be investigated in Section II-C. MSC design based on actual S0 ADL platforms will be discussed in Section II-E.

C. Multistrip Design for S0 Mode Acoustic Wave

After discussing the MSC fundamentals without specifying any acoustic modes, the multistrips will be designed for S0 in this section. To illustrate the characteristics of S0, the dispersion relations are first studied using the finite-element analysis (FEA) with COMSOL. An 800-nm-thick X-cut $LiNbO_3$ plate with 58 μm as one lateral dimension and the other lateral dimension ranging from 4 to 16 μm is studied using the approaches in [51]. Mechanically and electrically periodic boundary conditions are set to the vertical faces, and mechanically free boundary conditions are set to the top and bottom faces. The eigenfrequencies of S0 are plotted in Fig. 4(a). Eigen frequencies between 0.4 and 1.8 GHz are obtained for wavelengths between 4 and 16 μm for both the electrically short and open cases. For S0 at 1 GHz, the wavelength is around 6.2 μm. The phase velocities (v_p) are plotted in Fig. 4(b). The phase velocity for electrically open case (v_m) is around 7.2 km/s and that for electrically short case (v_f) is around 6.1 km/s, lower than v_m due to the piezoelectric stiffening [46]. k^2 of S0 is calculated using (3) and plotted in Fig. 4(c), showing a value no less than 35% for the S0 waves up to 1.6 GHz. More specifically, for our design frequency of 1 GHz, k^2 of S0 is 40.4%.

One of the major advantages of implementing S0 MSCs is that a given coupling function can be achieved with much fewer strips due to the significantly higher k^2 of S0. For instance, as shown in Fig. 3(c), a 3-dB hybrid coupler requires only 12 $\Lambda/8$ wide strips, while a full coupling requires 23 $\Lambda/8$ strips. Both numbers are less than 1/8 of that needed for a conventional SAW platform with k^2 of 5%.

Note that the significantly reduced number of strips introduces a new design challenge, namely the strong and wideband reflection induced by the multistrips. The multistrips, acting as acoustic gratings, show stopband characteristics at a wavelength around $4L_c$ [43]. Conventionally, SAW MSCs adopt strips with a width L_c of $\Lambda/5$ for separating the working frequency and the grating stopband [12]. However, such designs are not valid for S0 MSCs because of the wider stopband from fewer strips and the stronger reflection from each strip. On the one hand, the FBW of the stopband is inversely proportional to the number of elements in the array when the same reflectors are cascaded. Thus, the reduced number of strips leads to a wider stopband. On the other hand, the reflection from a single strip is more significant as a result of the more considerable mechanical reflection in the thin-film

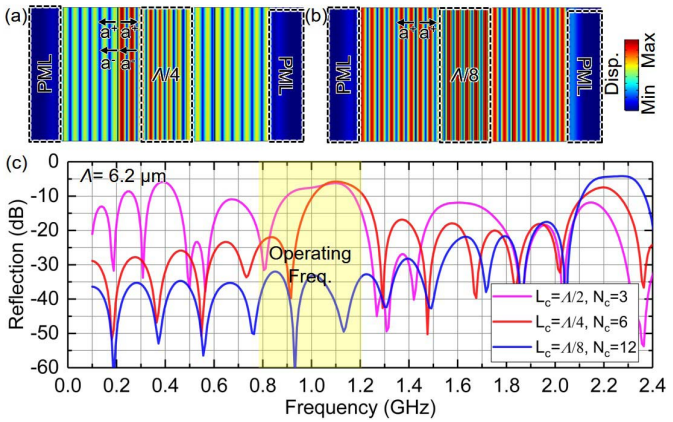

Fig. 5. Simulated reflection caused by the multistrips. Three sets of multistrips with different L_c but the same $L_c \cdot N_c$ are studied. Displacement mode shapes of (a) $\Lambda/4$ reflectors and (b) $\Lambda/8$ reflectors at 1 GHz. (c) Extracted reflection coefficient.

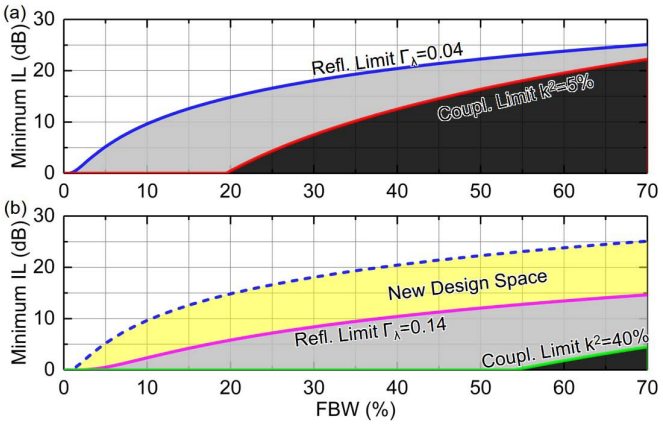

Fig. 6. Tradeoff between minimum IL and FBW for SPUDT ADLs in (a) conventional SAW and (b) S0-mode $LiNbO_3$ platform, showing forbidden regions from piezoelectric (black) and reflectivity limits (gray).

structure and larger electrical reflection induced by a larger k^2 [23].

One solution is to use pairs of $\Lambda/8$ strips. Due to the destructive interference of the reflected wave, their reflection for acoustic waves with a wavelength of Λ is eliminated [43]. To capture the intricacies in the multistrip design, frequency-domain FEA is performed for extracting the reflection coefficient of the 100-nm aluminum reflectors on the 800-nm $LiNbO_3$ [see Fig. 5(a) and (b)]. Floating potentials are applied to the interfaces between electrodes and $LiNbO_3$. Detailed simulation setups have been reported in [23] and [65]. In the simulation, an incident S0 wave propagates toward the multistrips. The multistrips have different L_c, but the same total length of $N_c \cdot L_c$ (1.5Λ), to ensure similar coupling (3-dB hybrid coupler) as discussed in Section II-B. Standing waves can be observed in the $\Lambda/4$ case but not in the $\Lambda/8$ case. The extracted mechanical reflection coefficient in Fig. 5(c) confirms the reflection suppression. Therefore, this work adopts $\Lambda/8$ strips, which do not require finer lithography resolution as the SPUDTs already use $\Lambda/8$ electrodes.

D. Design of S0 ADL Testbed

The previous discussions assume that RF signals are perfectly converted into mechanical waves at each port. However, efficient transduction at the ports is nontrivial. In fact, the excessive IL (>20 dB) or narrow FBW of the transducers are the bottlenecks for the conventional SAW MSCs. In this section, the S0 ADL testbed will be introduced, showing its great potential as a low-loss and wideband acoustic platform for MSCs.

The performance enhancement of S0 ADLs originates from the improved IL-FBW design space [45]. Two fundamental performance bounds exist for SPUDT ADLs, namely the piezoelectric coupling limit and the achievable reflectivity limit. In other words, the achievable IL and FBW are intertwined and have to be considered simultaneously. Both limitations have been discussed in detail in previous works [45], [49]. Thus, we will just briefly revisit this topic. The piezoelectric limitation sets the maximum 3-dB FBW for a device without significantly trading off IL, which is directly related to k^2 of an acoustic mode and the transducer design, presented as [45], [66]

$$\text{IL} = \text{FBW}^2 \cdot Q_T / c_{\text{piezo}}, \quad \text{when FBW} > \sqrt{c_{\text{piezo}}/Q_T} \tag{11}$$

$$c_{\text{piezo}} = \frac{v_f - v_m}{v_f} \cdot \left[1 + \frac{3(v_f - v_m)}{2v_f}\right] \tag{12}$$

where Q_T is the normalized transducer quality factor determined by the topology. c_{piezo} is the material piezoelectric constant determined by the material electromechanical coupling coefficient. For S0 with a wavelength of 6.2 μm, Q_T is 0.659 [66], and k^2 is 40.4%. The maximum FBW without introducing additional IL is 55%. The calculated limit coupling induced tradeoff is plotted in Fig. 6(b) in black. The reflectivity limitation is caused by finite unidirectionality from the embedded reflectors. To lower the IL, more reflectors, thus more cells, are needed, which inevitably leads to a narrower FBW for the transfer function of the SPUDT. Such a tradeoff can be expressed as

$$\text{IL} = 1 - e^{-\Gamma_\lambda/\text{FBW}} \tag{13}$$

$$\Gamma_\lambda = (\Gamma_m + \Gamma_e)/(1 + \Gamma_m \cdot \Gamma_e) \tag{14}$$

where Γ_λ is the reflection per wavelength, and Γ_m and Γ_e are the mechanically induced reflection and electrically induced reflection [23]. For our $3\pi/4$ distributed reflectors in S0 ADLs with 100-nm aluminum on 800-nm $LiNbO_3$, Γ_m is -0.038j, Γ_e is -0.105j, and Γ_λ is -0.144j [49]. The tradeoff is plotted in Fig. 6(b) in gray. Compared to the design space of a conventional SAW platform with k^2 of 5% and Γ_λ of $-0.04j$ [45] [see Fig. 6(a)], S0 platforms open up the low-loss, wideband design space. Specifically, for an 8% FBW design, the minimum achievable IL is improved from 8.1 to 1.6 dB, promising for lowering IL in MSCs.

To capture the design intricacies, four-port S0 ADL testbeds for MSCs are investigated using FEA (see Fig. 7). In the 3-D simulation, an 800-nm-thick $LiNbO_3$ plate is simulated with 100-nm-thick aluminum electrodes. The structure is assumed lossless, since the loss mechanisms of S0 are still under research [49], [67]. The transducers are placed and connected

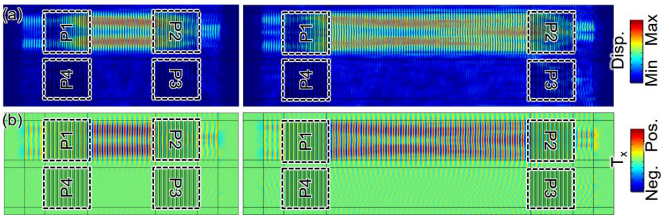

Fig. 7. Top views of the simulated (a) displacement and (b) stress (T_x) of the four-port ADL testbeds with L_g of 100 μm and 300 μm, respectively.

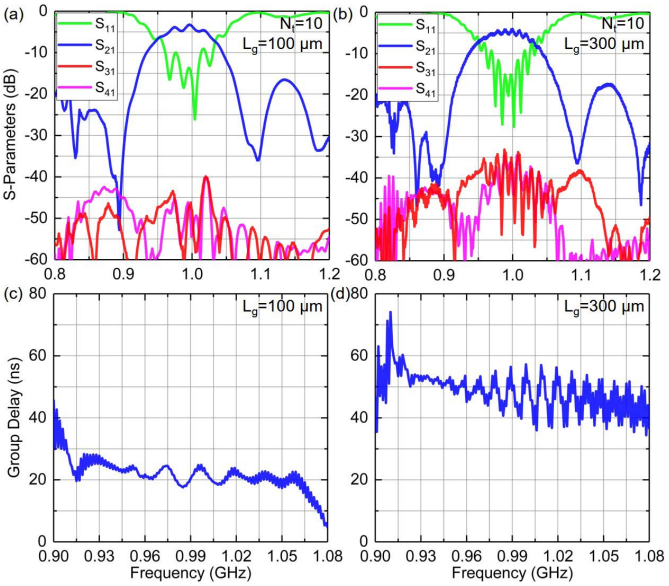

Fig. 8. Simulated performance of the four-port GHz S0 ADL testbeds with a cell length of 6.2 μm, 10 SPUDT cells, but different gap lengths of 100 μm and 300 μm. (a) and (b) IL. (c) and (d) Group delay.

to different ports based on Fig. 1. A cell number N_{tr} of 10 and a Λ of 6.2 μm are chosen. The aperture width W_a of each transducer is 58 μm, the total width W_d of the device is 149 μm, and the gap length L_g of the device is 100 μm and 300 μm, respectively. Free boundary conditions are set to the transverse ends, and perfectly matched layers (PML) are used at the longitudinal ends. The frequency-domain simulation is performed with Port 1 excited. The displacement and stress (T_x) distributions are presented in Fig. 7. Only top views are used here because S0 is uniform in the thickness direction. As seen in Fig. 7, RF signals are converted into acoustic waves at Port 1 and flow unidirectionally toward Port 2, thanks to the SPUDT. The generated acoustic waves flow toward Port 2, because of a near-zero PFA of S0 at this orientation (30° to $+Y$) [49]. After reaching Port 2, most of the acoustic energy are collected and converted back to RF.

The simulated S-parameters are shown in Fig. 8 for the cases with L_g of 100 μm and 300 μm. The ports are conjugately matched to $131 + j174\ \Omega$. The passband centers at 1 GHz, which is higher than the center frequencies of conventional SAW ADLs with similar feature sizes. This is due to the fast v_p of S0 (7 km/s compared to 3 km/s for the conventional SAW). A maximum S_{21} of -3.1 dB, a 3-dB FBW of 7.7%, a maximum S_{31} of -39.6 dB, a maximum S_{41} of

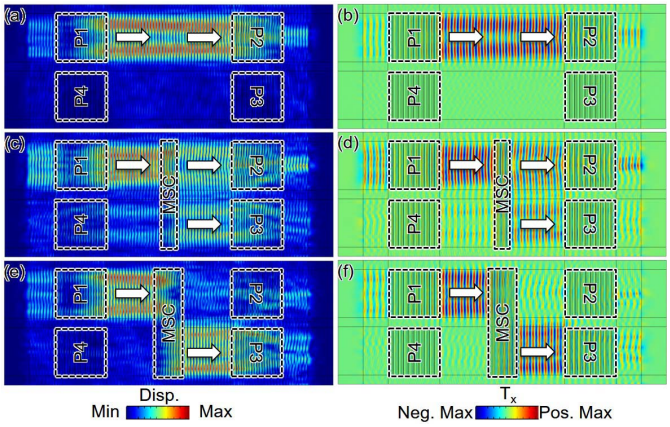

Fig. 9. Top views of the simulated displacement and stress (T_x) of the S0 MSC with L_g of 150 μm. (a) and (b) N_c of 0. (c) and (d) N_c of 11. (e) and (f) N_c of 21.

-39.8 dB, and a delay around 20 ns are obtained for the device with L_g of 100 μm. A maximum S_{21} of -3.9 dB, a 3-dB FBW of 8.2%, a maximum S_{31} of -33.1 dB, a maximum S_{41} of -34.5 dB, and a delay around 50 ns are obtained for the device with L_g of 300 μm. S_{21} is 1.5 dB lower than the predicted value [see (13)], mainly due to the fringe effects of the transducers. Both S_{21} and the isolation slightly degrade for longer ADLs, due to the slight diffraction of acoustic waves in the structure. Nevertheless, the isolations toward the coupled and isolated ports are adequate for showcasing MSCs. The ripples in S-parameters and group delays are caused by the finite directionality of the SPUDTs and can be further mitigated by using thicker electrodes [49]. The performance significantly outperforms the SAW ADLs in the IL-FBW tradeoff and the center frequency using the same feature size.

Note that ten-cell SPUDTs are used here for achieving couplers with sub-5-dB IL. If the design requirements are different, one can change the cell numbers for achieving different points on the IL-FBW tradeoff figure. For instance, with the same simulation setup, a five-cell ADL has an IL of 4.7 dB and a 3-dB FBW of 16.9%, while a 20-cell ADL has an IL of 1.9 dB, and a 3-dB FBW of 3.6%. For this work, ten-cell four-port ADLs will be used in the later sections.

E. Simulation of S0 MSC

Based on the multistrip and ADL designs, the performance of the entire S0 MSC is simulated through frequency-domain FEA. The multistrip simulation setup follows the description in Section II-C, and the ADL setup is the same as that in Section II-D. Different devices have the same L_g of 150 μm. S0 MSCs with different N_c between 0 and 27 are simulated. The mode shape and stress fields (T_x) are presented in Fig. 9 (N_c of 0, 11, and 21). As presented in Section II-D, the power flows from Port 1 to Port 2. With an increasing number of strips, more energy is coupled from Tracks A to B. When N_c is 11, the acoustic waves received at Port 2 and Port 3 are almost the same, which forms an acoustic hybrid coupler. As N_c increases, more energy flows to Port 3, and nearly all acoustic waves are transferred to Port 3 when N_c is 21.

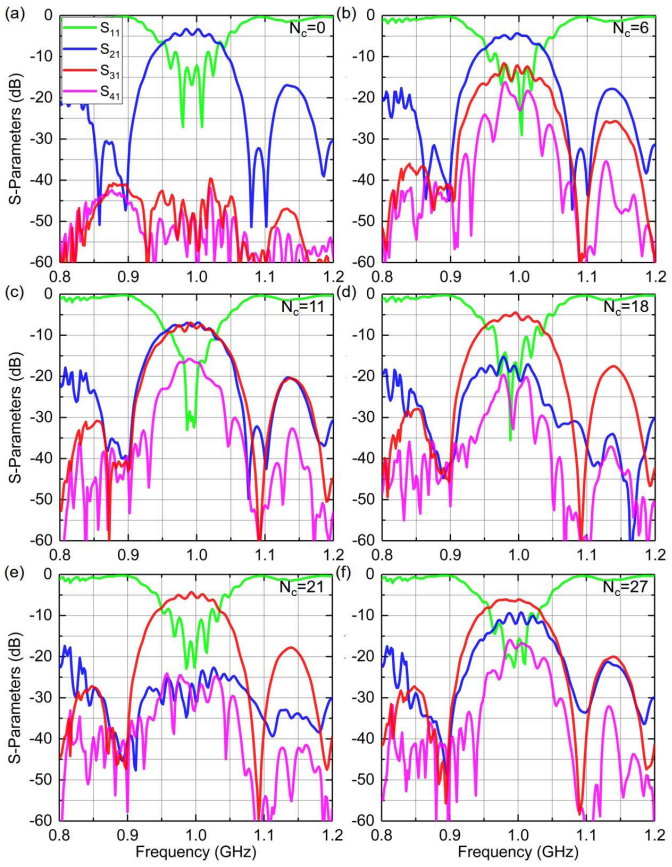

Fig. 10. Simulated S-parameters of S0 MSCs with different N_c. (a) $N_c = 0$. (b) $N_c = 6$. (c) $N_c = 11$. (d) $N_c = 18$. (e) $N_c = 21$. (f) $N_c = 27$.

The obtained S-parameters are shown in Fig. 10 for S0 MSCs with N_c of 0, 6, 11, 18, 21, and 27, when conjugately matched to $131 + j174\ \Omega$. Different devices show a 3-dB FBW of 8%. The simulated ADL testbed shows an IL of 3.3 dB, a coupling of 39.6 dB, and a coupling of 41.8 dB. The six-strip MSC shows an IL of 4.4 dB, a coupling of 11.7 dB, and a coupling of 16.2 dB. The 11-strip MSC has an IL of 7.1 dB, a coupling of 7.0 dB, and a coupling of 15.7 dB, which works as a hybrid coupler. The coupling keeps increasing for a larger N_c until N_c reaches 21. The 21-strip MSC has a coupling of 4.4 dB, an IL of 22.6 dB, and a coupling of 24.5 dB. The extra 1.1-dB IL in the track changer compared to the testbed is likely caused by the slight wave diffraction in the metal strips.

The simulated performance of different devices is summarized in Fig. 11. Directional couplers with different coupling can be achieved by employing different numbers of strips N_c. The calculated values from Fig. 3(b) are plotted in dashed lines. Compared with the ideal case, three differences are observed. First, a uniform loss around 3.3 dB exists in the FEA results, due to the unidirectional loss and diffraction loss in the ADL. Second, only finite isolation is attained due to the diffraction and the capacitive coupling between SPUDTs. Third, the full power transfer requires fewer strips predicted by calculation because the mechanical loading in the multistrips causes an even lower v_m in the metalized region [49], thus leading to a smaller N_T.

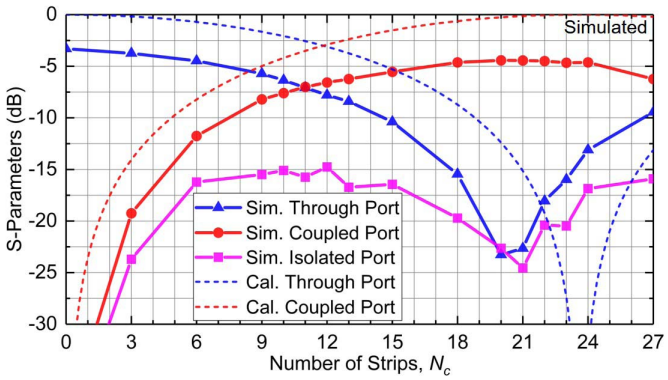

Fig. 11. Summary of FEA-simulated S-parameters. The theoretically calculated values are plotted in dashed lines.

F. 180° Hybrid Coupler for Enhanced Isolation

Fig. 11 shows that the isolation decays when the transmission is on par with the coupling. Specifically, the isolation of a 3-dB 90° hybrid coupler is only 15 dB, which is not desirable. The degradation of isolation originates from the partially reflected signal from SPUDTs due to the finite directionality of SPUDTs [49]. Such a process can be quantitatively explained using the S-parameter [see (8) and (9)] for an MSC with N_c less than N_T as

$$S = Ae^{-j\omega\delta} \times \begin{bmatrix} 0 & \cos(\theta_c/2) & j\cdot\sin(\theta_c/2) & 0 \\ \cos(\theta_c/2) & 0 & 0 & j\cdot\sin(\theta_c/2) \\ j\cdot\sin(\theta_c/2) & 0 & 0 & \cos(\theta_c/2) \\ 0 & j\cdot\sin(\theta_c/2) & \cos(\theta_c/2) & 0 \end{bmatrix} \tag{15}$$

where A is an amplitude constant. When all ports are terminated with the same mismatch factor of Γ_{port} introduced by SPUDTs, if Γ_{port} is small, the isolation can be approximated by

$$\left|S'_{41}\right| \approx A^2 \cdot |\Gamma_{\text{port}}| \cdot |\sin(\theta_c)| \tag{16}$$

where S'_{41} is the actual isolation observed at Port 4. The isolation follows the sinusoidal function with respect to N_c, and it reaches the maximum when N_c is half of N_T (3-dB 90° hybrid coupler). The trend is validated in Fig. 11. To enhance isolation, other than directly enhancing the directionality of SPUDTs, one can also implement devices with different phase relations between the through and coupled ports to cancel the reflection. One example is the 180° hybrid coupler [7]. Such a coupler can be built by offsetting the strips in Track B to be closer to Port 3 by $\Lambda/4$, while maintaining electrical connections to the strips in Track A [62]. The new design increases the phase difference between the through and coupled ports by $\pi/2$ for Ports 1 and 3, while reducing the phase difference by $\pi/2$ for Ports 2 and 4. The S-parameters for MSC 180° hybrid coupler are

$$S = Ae^{-j\omega\delta} \begin{bmatrix} 0 & 1 & -1 & 0 \\ 1 & 0 & 0 & -1 \\ -1 & 0 & 0 & 1 \\ 0 & -1 & 1 & 0 \end{bmatrix}. \tag{17}$$

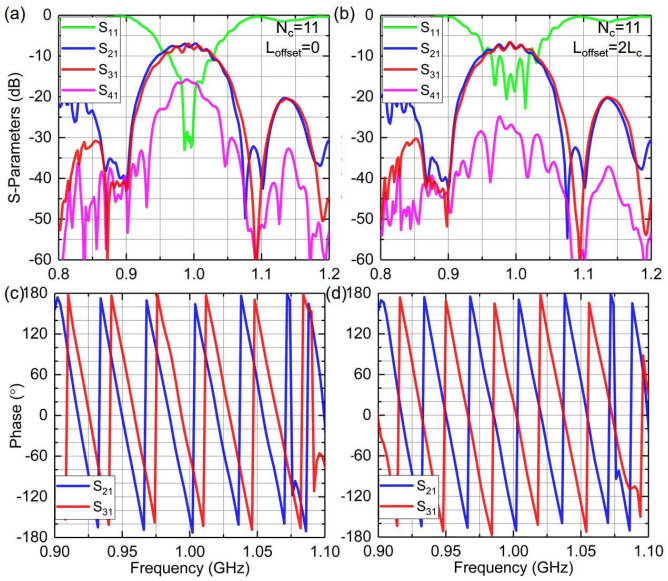

Fig. 12. Simulated (a) and (b) S-parameters and (c) and (d) phase of a 3-dB 90° hybrid MSC and a 3-dB 180° hybrid MSC.

Following the same assumption that all ports are terminated with the same mismatch factor of Γ_{port}, one can prove that S'_{41} is zero as the reflected waves from Ports 2 and 3 cancel out.

Note that such isolation enhancement is at the cost of a slight degradation in return loss (RL). Assuming small Γ_{port} introduced by SPUDTs, the RL can be approximated by

$$\left|S'_{11}\right| \approx A^2 \cdot |\Gamma_{\text{port}}| \cdot |\cos(\theta_c)| \tag{18}$$

where S'_{11} is the actual RL observed at Port 1. The reflection follows the cosinusoidal function with respect to N_c and reaches 0 when N_c is half of N_T (3-dB 90° hybrid coupler). On the contrary, the RL in the 180° hybrid coupler can be approximated by

$$\left|S'_{11}\right| \approx 2A^2 \cdot |\Gamma_{\text{port}}|. \tag{19}$$

The nonzero value leads to RL degradation.

The 180° hybrid MSC is simulated using the setup above and compared to the 90° hybrid MSC (see Fig. 12). In the simulation, N_c is 11, and the port impedance is $131 + j174\ \Omega$. Compared to the hybrid coupler, the 180° hybrid coupler has a significant isolation enhancement from 14.9 to 24.1 dB, while having an IL of 6.7 dB and a coupling of 6.5 dB over a 3-dB FBW of 8%. The slight degradation of RL is also observed for the 180° hybrid MSC. The phase of the coupled port is 93° larger than that of the through port for the 90° hybrid MSC, and the phase of the coupled port is 171° larger than that of the through port for the 180° hybrid MSC. The deviation of the phase difference from the calculated values is caused by the phase velocity difference in $LiNbO_3$ with and without electrodes. It can be adjusted by fine-tuning L_{offset}.

III. S0 Mode MSC Implementation

The devices were in-house fabricated with the process presented in [49]. An 800-nm X-cut $LiNbO_3$ thin film on a 4-inch Si wafer is provided by NGK Insulators, Ltd. for the fabrication. The optical images of the fabricated S0 MSCs are shown in Fig. 13. The key design parameters are labeled in the figure, and their typical values are shown in Table I.

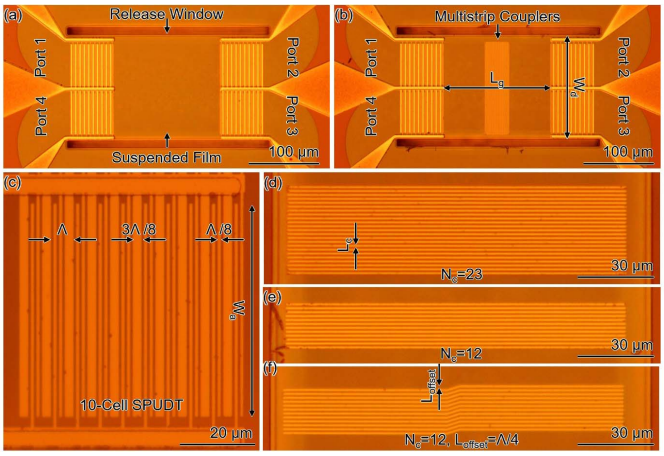

Fig. 13. Optical microscope images of the fabricated S0 MSCs. Zoomed-out views of (a) MSC testbed and (b) 23-strip MSC. (c) Zoomed-in view of one S0 SPUDT (Port 4). Zoomed-in views of the multistrips with (d) 23 Λ/8 strips, (e) 12 Λ/8 strips (track changer), and (f) 12 Λ/8 strips (90° hybrid MSC) and Λ/4 offset (180° hybrid MSC).

TABLE I
NOTATIONS OF MSC DIMENSIONS

Symbol	Parameter	Value	Symbol	Parameter	Value
Λ	Cell length (μm)	4.0-8.0	L_c	Strip length (μm)	0.775
W_a	Aperture width (μm)	58	W_d	Device width (μm)	149
L_g	Gap length (mm)	0.1-0.8	L_{offset}	Strip offset (μm)	1.55
N_{tr}	Number of cells	10	N_c	Number of strips	0-27
T_{LN}	$LiNbO_3$ thickness (nm)	800	T_{Al}	Aluminum thickness (nm)	100

TABLE II
KEY PARAMETERS OF THE FABRICATED DEVICES

Index	Cell Length, Λ (μm)	Gap Length, L_g (mm)	Cell No., N_{tr}	Strip No., N_c	Sim. (Fig.)	Meas. (Fig.)	Comments
Group A	6.2	0.1-0.8	10	0	8	14-15	S0 ADL testbeds
Group B	6.2	0.15	10	0-27	10-11	16-18	MSCs with diff. coupling
Group C	6.2	0.15	10	12	12	19	MSCs with diff. phase
Group D	4.0-8.0	0.15	10	12-24	-	20	MSCs at diff. freq.

Four groups of devices are implemented for investigating the design space of S0 MSCs (see Table II). Devices in Group A are four-port S0 ADL testbeds with different gap lengths, L_g, but otherwise the same as other S0 MSCs. This group is to identify the SPUDT performance and to extract the propagation characteristics of S0, including v_p and propagation loss (PL). Group B includes the GHz low-loss wideband S0 MSCs with different coupling. Group C contains the 180° hybrid MSCs with strips offset in the two tracks. Group D targets S0 MSCs at different frequencies, ranging

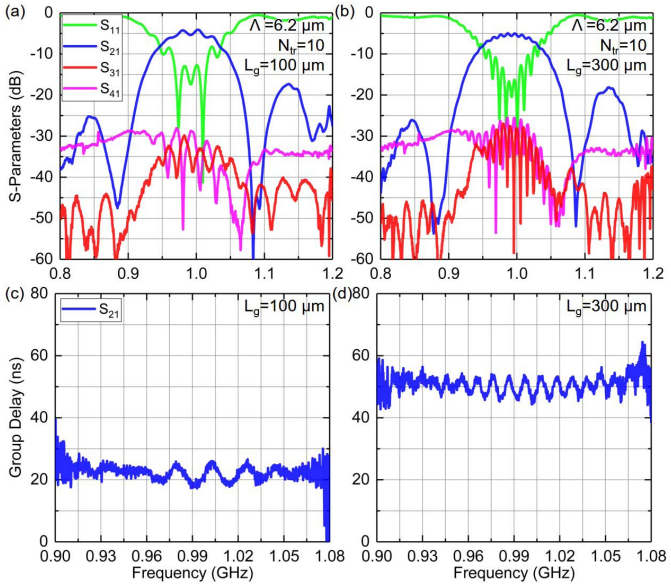

Fig. 14. Measured performance of the four-port GHz S0 ADL testbeds with a cell length of 6.2 μm, ten cells, but different gap lengths of 100 μm and 300 μm. (a) and (b) IL. (c) and (d) Group delay.

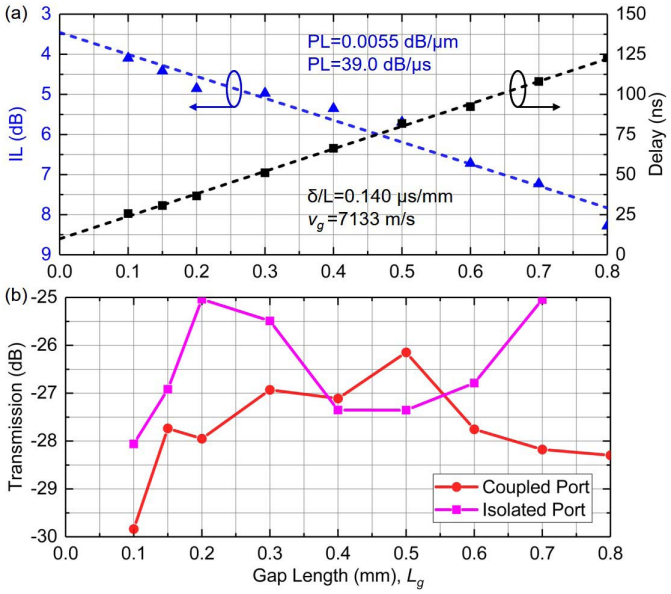

Fig. 15. Extracted S-parameters from ADLs in Group A. (a) IL versus L_g. (b) Transmission at the coupled and isolated port versus L_g. The extracted S0 propagation characteristics are also listed.

from 0.75 to 1.55 GHz. The measured results and discussion are presented in Section IV.

IV. Measurements and Discussion

A. S0 ADL Testbed

The fabricated devices were first measured with a performance network analyzer (Keysight N5249A PNA-X) at the −10-dBm power level in air. 40A-GS-200 probes from GGB Industries Inc. are used for on-chip measurement. GGB CS-2-200 differential calibration substrates are used to move the reference planes to the probe tips. The measurement results are then conjugately matched to $148 + j211\ \Omega$ in Keysight Advanced Design System. The four-port ADLs in Group A are designed for investigating the performance of the S0 ADL testbeds. They have the same Λ of 6.2 μm, N_{tr} of 10, but different L_g between 100 and 800 μm. The measured S-parameters and group delays of ADLs with L_g of 100 μm and 300 μm are plotted in Fig. 14. The 100-μm device shows an IL of 4.1 dB, a 3-dB FBW of 7.9%, a delay of 25 ns, and isolations around 28 dB for the isolated and coupled ports. The 300-μm device shows an IL of 4.9 dB, a 3-dB FBW of 7.9%, a delay of 51 ns, and isolations around 26 dB for the isolated and coupled ports.

The difference between the measured and the simulated IL is mainly caused by the PL. The IL and delay of different devices in Group A are summarized in Fig. 15(a). The PL and v_g in the acoustic waveguide are extracted using the slopes of IL and δ with respect to L_g. The PL of S0 in the waveguide is 0.0055 dB/μm or 39.0 dB/μs. The PL is larger than that obtained in the two-port S0 ADLs operating at the same frequency [49], likely caused by more severe diffraction in a structure with a large device width to aperture width ratio. The phase velocity is extracted as 7133 m/s, matching the simulated 7.2 km/s (see Fig. 4). The extracted parameters will be used to identify the loss contributions in Section IV-E.

The transmission at the coupled port and the isolated port of ADLs with different L_g is plotted in Fig. 15. The transmission to the coupled port is around −28 dB, and the isolation at the isolated port is around 26 dB. The isolation is worse than the simulated result by 10 dB, which is likely caused by the diffraction and capacitive coupling in the probing pad region. Nevertheless, these characterizations offer valuable experimental baselines. For instance, if measured coupling and isolation of S0 MSCs are above 26 dB, they are introduced by the multistrips but not by the ADLs upon which S0 MSCs are constructed.

B. S0 MSC With Different Coupling

Devices in Group B are designed for achieving acoustic couplers with different coupling factors. Group B includes MSCs with the same Λ of 6.2 μm, N_t of 10, L_g of 150 μm, and L_c of 0.775 μm but different N_c between 0 and 27. The measured S-parameters are presented in Fig. 16 for S0 MSCs with N_c of 0, 6, 12, 18, 23, and 27, and ports conjugately matched to $148 + j211\ \Omega$. Different devices show a 3-dB FBW of 8%. The measured testbed shows an IL of 4.5 dB, a coupling of 27.7 dB, and a coupling of 27.1 dB. The six-strip-MSC shows an IL of 5.1 dB, a coupling of 12.4 dB, and a coupling of 16.4 dB. The 12-strip-MSC has an IL of 7.5 dB, a coupling of 7.5 dB, and a coupling of 15.3 dB, which works as a hybrid coupler. Full power transfer happens when N_c is 23. 23-strip-MSC has a coupling of 5.1 dB, an IL of 24.3 dB, and a coupling of 22.6 dB, which is a track changer. Compared with the testbed, an extra 0.6-dB IL in the track changer is observed, likely due to the wave scattering and additional mechanical loss in the electrodes.

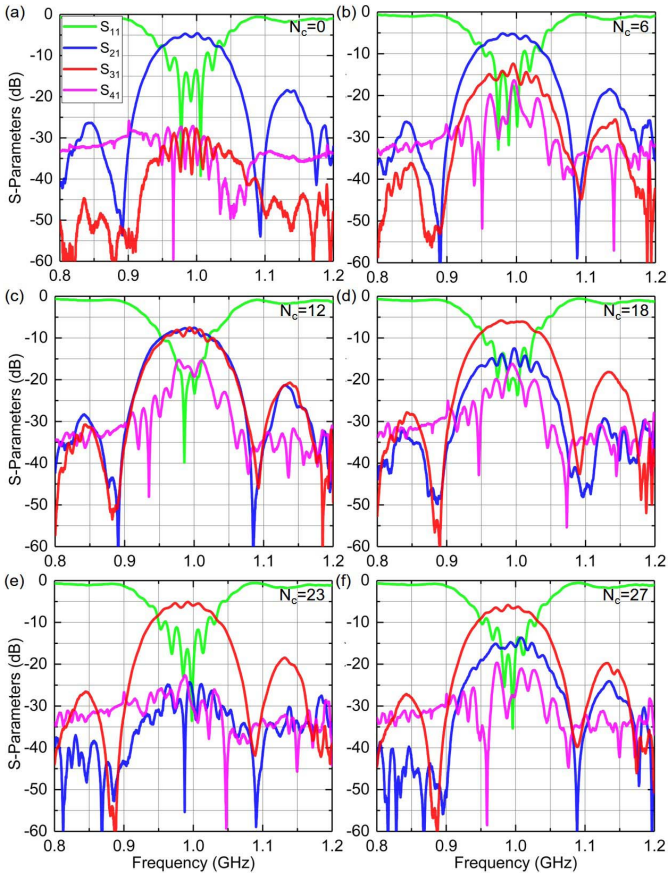

Fig. 16. Measured S-parameters of S0 MSCs with different N_c. (a) $N_c = 0$. (b) $N_c = 6$. (c) $N_c = 12$. (d) $N_c = 18$. (e) $N_c = 23$. (f) $N_c = 27$.

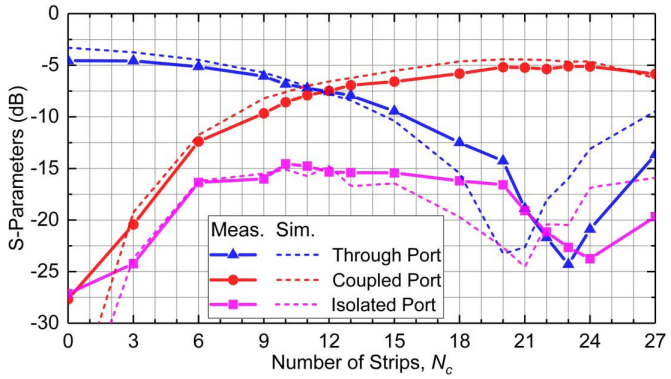

Fig. 17. Summary of the measured S-parameters. The results from FEA are plotted in dashed lines.

S-parameters of different devices in Group B are summarized in Fig. 17 and compared with the simulated values. The measured data follow the same trend as the simulated values. The major differences are found in the loss and the number of strips for full-energy transfer between tracks. The 1.2-dB additional loss in the measurement is mainly due to PL. Detailed analysis of IL contributors is presented in Section IV-E. The difference in the periodicity relative to the number of strips is likely caused by the slight difference between the material properties used in FEA and those got in the implementation.

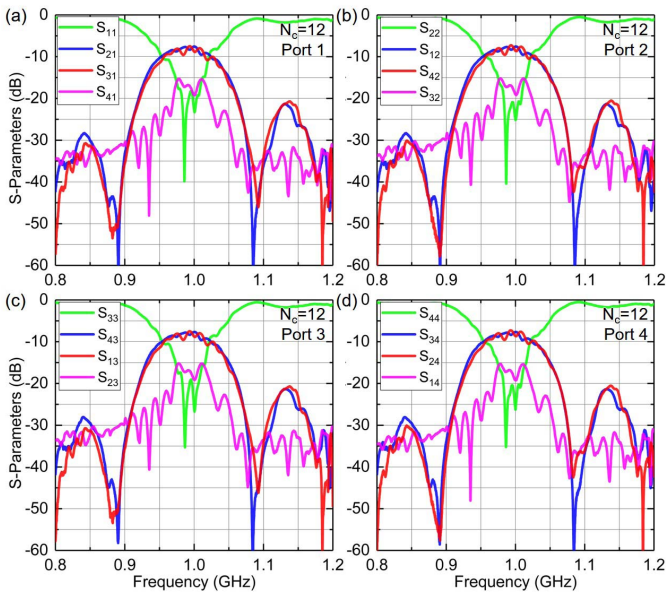

Fig. 18. Measured S-parameters of S0 MSCs with N_c of 12 at (a) Port 1, (b) Port 2, (c) Port 3, and (d) Port 4.

The complete set of S-parameter of the 3-dB 90° hybrid coupler ($N_c = 12$) is presented in Fig. 18. Excellent symmetry among ports has been achieved.

The measurement in this section validates our MSC designs, showing that acoustic directional couplers can be implemented in S0 platforms with compact footprint and achieving better IL-FBW tradeoff. The design flexibility of couplers with different coupling is also showcased.

C. 180° Hybrid Coupler for Enhanced Isolation

From Fig. 17, one can observe that the isolation degrades for a 3-dB 90° hybrid MSC, which agrees with that predicted in Section II-F. To enhance the isolation for the 3-dB acoustic coupler, the 3-dB 180° hybrid MSC (Group C) is built.

The comparison between the S-parameters of the two devices ($N_c = 12$, $\Lambda = 6.2$ μm, different L_{offset}) is shown in Fig. 19. The ports are conjugately matched to $148 + j211$ Ω. The isolation is enhanced from 15.3 to 20.8 dB, with a local minimum less than 40 dB in the center frequency, while showing an IL of 7.7 dB and a coupling of 7.6 dB with a 3-dB FBW of 8%. The phase of the coupled port is 93° larger than that of the through port for the 90° hybrid MSC, and the phase of the coupled port is 168° larger than that of the through port for the 180° hybrid MSC. The values are very close to those obtained from FEA. The deviation from the ideal case (180°) can be mitigated in future designs by fine-tuning L_{offset}, and the isolation can be further improved in that case.

D. S0 MSC With Different Center Frequencies

Devices in Group D are designed with different Λ (8.0, 5.0, and 4.0 μm) to show the frequency scalability of S0 MSCs. The measured response of hybrid couplers and track changers at different frequencies are plotted in Fig. 20.

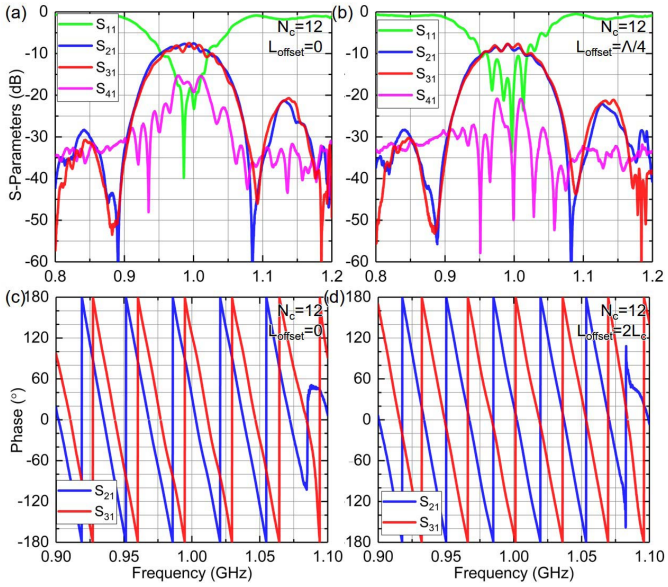

Fig. 19. Measured (a) and (b) S-parameters and (c) and (d) phase of a 3-dB 90° hybrid MSC and a 3-dB 180° hybrid MSC.

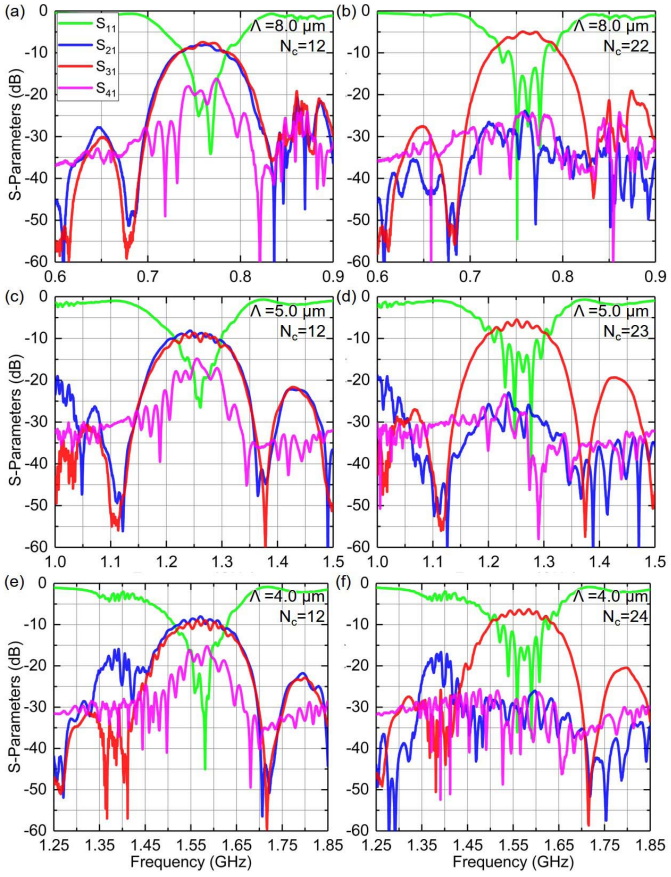

Fig. 20. Measured S-parameters of S0 MSCs at different frequencies. (a) N_c of 12, Λ of 8.0 μm. (b) N_c of 22, Λ of 8.0 μm. (c) N_c of 12, Λ of 5.0 μm. (d) N_c of 23, Λ of 5.0 μm. (e) N_c of 12, Λ of 4.0 μm. (f) N_c of 24, Λ of 4.0 μm.

The devices at 0.75 GHz ($\Lambda = 8.0$ μm) are conjugately matched to $297 + j223$ Ω. The 3-dB hybrid MSC ($N_c = 12$) shows an IL of 8.0 dB and a coupling of 7.4 dB, while the track changer ($N_c = 22$) shows an IL of 4.9 dB. The devices at 1.25 GHz ($\Lambda = 5.0$ μm) are conjugately matched to $200 + j102$ Ω. The 3-dB hybrid MSC ($N_c = 12$) shows an IL of 8.1 dB and a coupling of 8.6 dB, while the track changer ($N_c = 23$) shows an IL of 5.4 dB. The devices at 1.55 GHz ($\Lambda = 4.0$ μm) are conjugately matched to $151 + j81$ Ω. The 3-dB hybrid MSC ($N_c = 12$) shows an IL of 8.0 dB and a coupling of 8.9 dB, while the track changer ($N_c = 24$) shows an IL of 6.2 dB. All devices have similar FBW of 8%.

TABLE III
EXAMPLES OF LOSS BREAKDOWN IN S0 MSCS

Damping Source	Testbed (N_c=0)	3-dB coupler (N_c=12)	Track changer (N_c=23)
Finite Uni-directionality	3.1 dB	3.1 dB	3.1 dB
Propagation Loss	1.1 dB	1.1 dB	1.1 dB
Loss in Multistrips & Other	0.3 dB	0.3 dB	0.9 dB
Total Loss	4.5 dB	4.5 dB	5.1 dB

Two major differences are notable when comparing the performance of devices at different frequencies. First, fewer strips are required for achieving the same function at lower frequencies, which is caused by the dispersive k^2 of S0 in the thin film (see Fig. 4). The larger k^2 of S0 at lower frequencies leads to a smaller N_T. Thus, fewer strips are needed for the same function. Second, the loss is less at lower frequencies, which is caused by the increasing PL of S0 at higher frequencies [49]. Therefore, these factors should be considered when designing for S0 MSCs at different frequencies.

Moreover, the MSCs also selectively filter out the spurious modes with smaller k^2 in the coupler port, because the number of strips are not adequate to enable energy transfer between tracks for modes with low k^2. In this case, the A0 mode near the S0 passband, which is more obvious for the current film stack above 1.0 GHz [49], is filtered out in the coupled signal. This results from the remarkably different k^2 of S0 and A0 in $LiNbO_3$. Such characteristics can also be used to suppress adjacent spurious modes, which mostly have lower k^2 than the main mode [12].

E. IL Breakdown and Discussion

Based on the FEA simulation validated by the measurement and the experimentally extracted parameters, the loss in S0 MSCs can be broken down for identifying the space for future improvement (see Table III). Most loss in S0 MSCs originates from the S0 ADL testbed. The unidirectional loss of 3.1 dB is the most significant contributor. It can be reduced by enhancing the reflectivity per cell in SPUDTs by using thicker electrodes for larger mechanical reflection [23], [45]. A sub-1.5-dB unidirectional loss is feasible [56]. The 1.1-dB PL in the waveguide is the second loss source, from the 150-μm waveguide and 62-μm equivalent propagation distance in the SPUDTs [23]. However, the compact structure of the multistrips only requires less than 40 μm in the longitudinal direction for the track changer. Therefore, one can expect a sub-0.5-dB loss in a shorter ADL with the same functions. The remaining loss is likely caused by the multistrips and

other sources such as diffraction. The source will be further identified when the major damping terms are lowered in future demonstrations. To sum up, sub-2-dB S0 MSCs are feasible upon further optimization.

One major improvement in future implementations is the isolation of the couplers. As discussed in Section II-F, the isolation degradation originates from the port reflection due to the in-adequate directionality of the SPUDTs. To enhance directionality, several approaches are viable. First, larger reflection per wavelength can be obtained with thicker electrodes or heavier metal [23]. Second, it is possible to further mitigate the reflections using more unit cells in the transducers at the cost of FBW [49]. Another issue in the current prototypes is the in-band ripples. Two factors contribute to the ripples, namely the standing waves in the waveguide and the intrinsically weak resonances in the SPUDT. For future implementations, the first source can be mitigated by the same approaches for lowering the unidirectional loss. The second aspect can be improved by optimizing the reflection and reflection simultaneously across the entire transducers [68]. Finally, the power handling capability might be a potential issue because the energy is concentrated in a much more compact volume [see Fig. 3(a)], leading to thermally induced nonlinearity in $LiNbO_3$ thin films [69]. Currently, the device shows no performance degradation at 5 dBm (maximum power of the measurement setup). The power-handling capability can be further improved in future implementations by including tethers at the release windows in the transverse direction, which leads to better thermal conductance.

V. Conclusion

In this work, we have demonstrated low-loss, wideband RF couplers using the thin-film $LiNbO_3$. The fabricated S0 MSCs significantly improves the IL and operating frequency in a more compact structure compared to the previous works, because of the simultaneously large k^2, high v_p, and low loss of the S0 mode in $LiNbO_3$. Devices with different coupling (20–3 dB) are fabricated using various numbers of strips. Based on the S0 testbed with an IL of 4.5 dB at 1 GHz, the hybrid coupler shows an IL of 7.5 dB, while the track changer shows an IL of 5.1 dB, over a 3-dB FBW of 8%. Couplers at different frequencies (between 0.75 and 1.55 GHz) are also investigated. Upon further optimizations, the demonstrated couplers can be potentially crucial elements to complete an RF acoustic component kit for portable RF front ends.

References

[1] G. Marconi, "Wireless telegraphic communication," *Reson*, vol. 7, no. 1, pp. 95–101, Jan. 2002.

[2] D. Tse and P. Viswanath, *Fundamentals of Wireless Communication*. Cambridge, U.K.: Cambridge Univ. Press, 2005.

[3] M. I. Skolnik, *Introduction to Radar Systems*. New York, NY, USA: McGraw-Hill, 1980, p. 590.

[4] M. Cooper *et al.*, "Radio telephone system," U.S. Patents 3 906 166, Sep. 16, 1975.

[5] S. Parkvall, E. Dahlman, A. Furuskar, and M. Frenne, "NR: The new 5G radio access technology," *IEEE Commun. Standards Mag.*, vol. 1, no. 4, pp. 24–30, Dec. 2017.

[6] P. Warder and A. Link, "Golden age for filter design: Innovative and proven approaches for acoustic filter, duplexer, and multiplexer design," *IEEE Microw. Mag.*, vol. 16, no. 7, pp. 60–72, Aug. 2015.

[7] D. M. Pozar, *Microwave Engineering*. Hoboken, NJ, USA: Wiley, 2009.

[8] R. Ruby, "A snapshot in time: The future in filters for cell phones," *IEEE Microw. Mag.*, vol. 16, no. 7, pp. 46–59, Aug. 2015.

[9] R. Ruby, P. Bradley, D. Clark, D. Feld, T. Jamneala, and K. Wang, "Acoustic FBAR for filters, duplexers and front end modules," in *IEEE MTT-S Int. Microw. Symp. Dig.*, vol. 2, Nov. 2004, pp. 931–934.

[10] T. Kimura, M. Omura, Y. Kishimoto, and K. Hashimoto, "Comparative study of acoustic wave devices using thin piezoelectric plates in the 3–5-GHz range," *IEEE Trans. Microw. Theory Techn.*, vol. 67, no. 3, pp. 915–921, Jan. 2019.

[11] G. G. Fattinger *et al.*, "Carrier aggregation and its challenges-or: The golden age for acoustic filters," in *IEEE MTT-S Int. Microw. Symp. Dig.*, May 2016, pp. 1–4.

[12] F. G. Marshall, C. O. Newton, and E. G. S. Paige, "Surface acoustic wave multistrip components and their applications," *IEEE Trans. Microw. Theory Techn.*, vol. 21, no. 4, pp. 216–225, Apr. 1973.

[13] F. G. Marshall, C. O. Newton, and E. G. S. Paige, "Theory and design of the surface acoustic wave multistrip coupler," *IEEE Trans. Microw. Theory Techn.*, vol. MTT-21, no. 4, pp. 206–215, Apr. 1973.

[14] W. L. Bond, J. H. Collins, H. M. Gerard, T. M. Reeder, and H. J. Shaw, "Acoustic surface wave coupling across an air gap," *Appl. Phys. Lett.*, vol. 14, no. 4, pp. 122–124, Feb. 1969.

[15] E. Ash and D. Morgan, "Realisation of microwave-circuit functions using acoustic surface waves," *Electron. Lett.*, vol. 3, no. 10, pp. 462–464, Oct. 1967.

[16] H. Herrmann, U. Rust, and K. Schafer, "Tapered acoustical directional couplers for integrated acousto-optical mode converters with weighted coupling," *J. Lightw. Technol.*, vol. 13, no. 3, pp. 364–374, Mar. 1995.

[17] L. Solie and M. Wohlers, "Use of an saw multiplexer in FMCW radar system," *IEEE Trans. Microw. Theory Techn.*, vol. 29, no. 5, pp. 419–423, May 1981.

[18] H. Van De Vaart and L. Solie, "Surface-acoustic-wave multiplexing techniques," *Proc. IEEE*, vol. 64, no. 5, pp. 688–691, 1976.

[19] T. Manzaneque, R. Lu, Y. Yang, and S. Gong, "Lithium niobate MEMS chirp compressors for near zero power wake-up radios," *J. Microelectromech. Syst.*, vol. 26, no. 6, pp. 1204–1215, Dec. 2017.

[20] S. Ghosh and J. Cafarella, "SAW correlators in $LiNbO_3$ and GaN on sapphire," in *Proc. IEEE Int. Freq. Control Symp.*, May 2018, pp. 1–4.

[21] W. Smith, H. Gerard, J. Collins, T. Reeder, and H. Shaw, "Design of surface wave delay lines with interdigital transducers," *IEEE Trans. Microw. Theory Techn.*, vol. MTT-17, no. 11, pp. 865–873, Nov. 1969.

[22] G. Vidal-Álvarez, A. Kochhar, and G. Piazza, "Delay lines based on a suspended thin film of X-cut lithium niobate," in *Proc. IEEE Int. Ultrason. Symp.*, Sep. 2017, pp. 1–4.

[23] T. Manzaneque, R. Lu, Y. Yang, and S. Gong, "Low-loss and wideband acoustic delay lines," *IEEE Trans. Microw. Theory Techn.*, vol. 67, no. 4, pp. 1379–1391, Apr. 2019.

[24] R. Lu, Y. Yang, M. Li, M. Breen and S. Gong, "5-GHz antisymmetric mode acoustic delay lines in lithium niobate thin film," *IEEE Trans. Microw. Theory Techn.*, vol. 68, no. 2, pp. 573–589, Feb. 2020.

[25] R. Lu, S. Link, and S. Gong, "A unidirectional transducer design for scaling GHz AlN-based RF microsystems," *IEEE Trans. Ultrason., Ferroelectr., Freq. Control*, to be published.

[26] D. Ciplys *et al.*, "GaN-based SAW delay-line oscillator," *Electron. Lett.*, vol. 37, no. 8, pp. 545–546, 2001.

[27] M. Li, R. Lu, T. Manzaneque, and S. Gong, "Low phase noise RF oscillators based on thin-film lithium niobate acoustic delay lines," *J. Microelectromech. Syst.*, to be published.

[28] S. Ghosh, M. A. Hollis, and R. J. Molnar, "Acoustoelectric amplification of Rayleigh waves in low sheet density AlGaN/GaN heterostructures on sapphire," *Appl. Phys. Lett.*, vol. 114, no. 6, Feb. 2019, Art. no. 063502.

[29] L. Hackett *et al.*, "High-gain leaky surface acoustic wave amplifier in epitaxial InGaAs on lithium niobate heterostructure," *Appl. Phys. Lett.*, vol. 114, no. 25, Jun. 2019, Art. no. 253503.

[30] S. Ghosh *et al.*, "Nonreciprocal acoustoelectric interaction of surface waves and fluorine plasma-treated AlGan/GaN 2DEG," in *Proc. Transducers*, 2017, pp. 1939–1942.

[31] D. C. Malocha, C. Carmichael, M. S. Smith, and A. Weeks, "Thin film acoustoelectric GHz SAW amplifier design," in *Proc. IEEE Int. Ultrason. Symp. (IUS)*, Oct. 2018, pp. 1–4.

[32] R. Lu, T. Manzaneque, Y. Yang, and S. Gong, "Exploiting parallelism in resonators for large voltage gain in low power wake up radio front ends," in *Proc. IEEE Int. Conf. Micro Electro Mech. Syst.*, vol. 2018, pp. 747–750.

[33] L. Colombo, A. Kochhar, G. Vidal-Alvarez, and G. Piazza, "X-cut lithium niobate laterally vibrating MEMS resonator with figure of merit of 1560," *J. Microelectromech. Syst.*, vol. 27, no. 4, pp. 602–604, Aug. 2018.

[34] R. H. Olsson, K. E. Wojciechowski, M. R. Tuck, and J. E. Stevens, "Microresonant impedance transformers," in *Proc. IEEE Int. Ultrason. Symp.*, Sep. 2009, pp. 2153–2157.

[35] S. S. Bedair, J. S. Pulskamp, R. G. Polcawich, B. Morgan, J. L. Martin, and B. Power, "Thin-film piezoelectric-on-silicon resonant transformers," *J. Microelectromech. Syst.*, vol. 22, no. 6, pp. 1383–1394, Dec. 2013.

[36] R. Lu, T. Manzaneque, Y. Yang, L. Gao, A. Gao, and S. Gong, "A radio frequency nonreciprocal network based on switched acoustic delay lines," *IEEE Trans. Microw. Theory Techn.*, vol. 67, no. 4, pp. 1516–1530, Apr. 2019.

[37] Y. Yu et al., "Radio frequency magnet-free circulators based on spatiotemporal modulation of surface acoustic wave filters," 2019, *arXiv:1905.13252*. [Online]. Available: https://arxiv.org/abs/1905.13252

[38] M. M. Torunbalci, T. J. Odelberg, S. Sridaran, R. C. Ruby, and S. A. Bhave, "An FBAR Circulator," *IEEE Microw. Wireless Compon. Lett.*, vol. 28, no. 5, pp. 395–397, May 2018.

[39] M. A. Kemp *et al.*, "A high Q piezoelectric resonator as a portable VLF transmitter," *Nature Commun.*, vol. 10, no. 1, 2019, Art. no. 1715.

[40] A. E. Hassanien, M. Breen, M.-H. Li, and S. Gong, "Acoustically driven and modulation inducible radiating elements," 2019, *arXiv:1906.07797*. [Online]. Available: https://arxiv.org/abs/1906.07797

[41] T. Nan *et al.*, "Acoustically actuated ultra-compact NEMS magnetoelectric antennas," *Nature Commun.*, vol. 8, no. 1, p. 296, Aug. 2017.

[42] H. Bhugra and G. Piazza, *Piezoelectric MEMS Resonators and Filters*. Cham, Switzerland: Springer, 2017.

[43] K. Hashimoto, *Surface Acoustic Wave Devices in Telecommunications: Modelling and Simulation*. Berlin, Germany: Springer-Verlag, 2013.

[44] M. Pijolat *et al.*, "Large Qxf product for HBAR using smart cut transfer of $LiNbO_3$ thin layers onto $LiNbO_3$ substrate," in *Proc. IEEE Int. Ultrason. Symp.*, Nov. 2008, pp. 201–204.

[45] C. S. Hartmann and B. P. Abbott, "Overview of design challenges for single phase unidirectional SAW filters," in *Proc. IEEE Int. Ultrason. Symp.*, Jan. 1989, pp. 79–89.

[46] H. Jaffe and D. A. Berlincourt, "Piezoelectric transducer materials," *Proc. IEEE*, vol. 53, no. 10, pp. 1372–1386, Oct. 1965.

[47] S. Gong and G. Piazza, "Design and analysis of lithium-niobate-based high electromechanical coupling RF-MEMS resonators for wideband filtering," *IEEE Trans. Microw. Theory Techn.*, vol. 61, no. 1, pp. 403–414, Jan. 2013.

[48] R. Wang, S. A. Bhave, and K. Bhattacharjee, "Design and fabrication of S_0 Lamb-wave thin-film lithium niobate micromechanical resonators," *J. Microelectromech. Syst.*, vol. 24, no. 2, pp. 300–308, Apr. 2015.

[49] R. Lu, T. Manzaneque, Y. Yang, M.-H. Li, and S. Gong, "Gigahertz low-loss and wideband S_0 mode lithium niobate acoustic delay lines," *IEEE Trans. Ultrason., Ferroelectr., Freq. Control*, vol. 66, no. 8, pp. 1373–1386, Aug. 2019.

[50] R. H. Olsson *et al.*, "A high electromechanical coupling coefficient SH_0 Lamb wave lithium niobate micromechanical resonator and a method for fabrication," *Sens. Actuators A, Phys.*, vol. 209, pp. 183–190, Mar. 2014.

[51] R. Lu, Y. Yang, M.-H. Li, T. Manzaneque, and S. Gong, "GHz broadband SH_0 mode lithium niobate acoustic delay lines," *IEEE Trans. Ultrason., Ferroelectr., Freq. Control*, vol. 67, no. 2, pp. 402–412, Feb. 2020.

[52] C. J. Sarabalis, Y. D. Dahmani, A. Y. Cleland, and A. H. Safavi-Naeini, "The role of resonance and bandgaps in high $k_{eff}{}^2$ transducers," 2019, *arXiv:1904.04981*. [Online]. Available: https://arxiv.org/abs/1904.04981

[53] M. Kadota, T. Ogami, K. Yamamoto, H. Tochishita, and Y. Negoro, "High-frequency lamb wave device composed of MEMS structure using $LiNbO_3$ thin film and air gap," *IEEE Trans. Ultrason., Ferroelectr., Freq. Control*, vol. 57, no. 11, pp. 2564–2571, Nov. 2010.

[54] V. Plessky, S. Yandrapalli, P. Turner, L. Villanueva, J. Koskela, and R. Hammond, "5 GHz laterally-excited bulk-wave resonators (XBARs) based on thin platelets of lithium niobate," *Electron. Lett.*, vol. 55, no. 2, pp. 98–100, Jan. 2019.

[55] Y. Yang, A. Gao, R. Lu, and S. Gong, "5 GHz lithium niobate MEMS resonators with high FoM of 153," in *Proc. IEEE Int. Conf. Micro Electro Mech. Syst*, Jan. 2017, pp. 942–945.

[56] R. Lu, T. Manzaneque, Y. Yang, and S. Gong, "S_0-mode lithium niobate acoustic delay lines with 1 dB insertion loss," in *Proc. IEEE Int. Ultrason. Symp.*, Oct. 2018, pp. 1–9.

[57] E. Jones, "Coupled-strip-transmission-line filters and directional couplers," *IEEE Trans. Microw. Theory Techn.*, vol. MTT-4, no. 2, pp. 75–81, Apr. 1956.

[58] C. Pon, "Hybrid-ring directional coupler for arbitrary power divisions," *IEEE Trans. Microw. Theory Techn.*, vol. MTT-9, no. 6, pp. 529–535, Nov. 1961.

[59] E. A. J. Marcatili, "Dielectric rectangular waveguide and directional coupler for integrated optics," *Bell Syst. Tech. J.*, vol. 48, no. 7, pp. 2071–2102, Sep. 1969.

[60] E. Wilkinson, "An N-way hybrid power divider," *IEEE Trans. Microw. Theory Techn.*, vol. MTT-8, no. 1, pp. 116–118, Jan. 1960.

[61] F. Marshall and E. Paige, "Novel acoustic-surface-wave directional coupler with diverse applications," *Electron. Lett.*, vol. 7, no. 16, pp. 460–462, 1971.

[62] H. Becker, C. Rupp, M. Von Schickfus, and S. Hunklinger, "Multistrip couplers for surface acoustic wave sensor application," *IEEE Trans. Ultrason., Ferroelectr., Freq. Control*, vol. 43, no. 4, pp. 527–530, Jul. 1996.

[63] *IEEE Standard on Piezoelectricity*, IEEE Standard ANSI/IEEE Std 176-1987, 1988.

[64] R. Lu, M.-H. Li, Y. Yang, T. Manzaneque, and S. Gong, "Accurate extraction of large electromechanical coupling in piezoelectric MEMS resonators," *J. Microelectromech. Syst.*, vol. 28, no. 2, pp. 209–218, Apr. 2019.

[65] R. Lu, T. Manzaneque, Y. Yang, and S. Gong, "Lithium niobate phononic crystals for tailoring performance of RF laterally vibrating devices," *IEEE Trans. Ultrason., Ferroelectr., Freq. Control*, vol. 65, no. 6, pp. 934–944, Jun. 2018.

[66] C. S. Hartmann, S. Jen, M. A. Domalewski, and J. C. Andle, "Improved accuracy for determining SAW transducer capacitance and k^2," in *Proc. IEEE Int. Ultrason. Symp*, Oct. 1987, pp. 161–168.

[67] I. L. Bajak, A. Mcnab, J. Richter, and C. D. W. Wilkinson, "Attenuation of acoustic waves in lithium niobate," *J. Acoust. Soc. Amer.*, vol. 69, no. 3, pp. 689–695, Mar. 1981.

[68] J. M. Hodé, J. Desbois, P. Difilie, M. Solal, and P. Ventura, "SPUDT-based filters: Design principles and optimization," in *Proc. IEEE Int. Ultrason. Symp.*, Nov. 1995, pp. 39–50.

[69] R. Lu and S. Gong, "Study of thermal nonlinearity in lithium niobate-based MEMS resonators," in *Proc. Transducers*, Jun. 2015, pp. 1993–1996.

Ruochen Lu (Member, IEEE) received the B.E. degree (Hons.) in microelectronics from Tsinghua University, Beijing, China, in 2014 and the M.S. and Ph.D. degrees in electrical engineering from the University of Illinois at Urbana–Champaign (UIUC), Urbana, IL, USA, in 2017 and 2019, respectively.

He is currently a Postdoctoral Researcher with UIUC. His research interests include radio frequency microsystems and their applications for timing and signal processing.

Dr. Lu received the Best Student Paper Awards at the 2017 IEEE International Frequency Control Symposium and the 2018 IEEE International Ultrasonics Symposium. He is also a recipient of the 2015 Lam Graduate Award from the College of Engineering, UIUC, the 2017 Nick Holonyak, Jr. Graduate Research Award, the 2018 Nick Holonyak, Jr. Fellowship, and the 2019 Raj Mittra Outstanding Research Award from the Department of Electrical and Computer Engineering, UIUC.

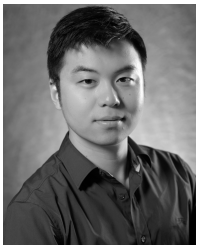

Yansong Yang (Member, IEEE) received the B.S. degree in electrical and electronic engineering from the Huazhong University of Science and Technology, Wuhan, China, in 2014 and the M.S. and Ph.D. degrees in electrical engineering from the University of Illinois at Urbana–Champaign (UIUC), Urbana, IL, USA, in 2017 and 2019, respectively.

He is currently a Postdoctoral Researcher with UIUC. His research interests include design and microfabrication techniques of RF MEMS resonators, filters, switches, and photonic integrated circuits.

Dr. Yang received the Second Place in the Best Paper Competition at the 2018 IEEE International Microwave Symposium and the Best Paper Award from the 2019 IEEE International Ultrasonics Symposium. He was also a finalist of the Best Paper Award in the 2018 IEEE International Frequency Control Symposium. He is also a recipient of the 2019 P. D. Coleman Graduate Research Award from the Department of Electrical and Computer Engineering, UIUC.

Ming-Huang Li (Member, IEEE) received the B.S. degree in mechanical engineering (minor in electrical engineering) from National Chung Cheng University, Chiayi, Taiwan, in 2009 and the M.S. and Ph.D. degrees from the Institute of NanoEngineering and MicroSystems, National Tsing Hua University (NTHU), Hsinchu, Taiwan, in 2011 and 2015, respectively.

He was with Micro and Nanotechnology Laboratory, University of Illinois at Urbana–Champaign, Urbana, IL, USA, as a Postdoctoral Researcher. He is currently an Assistant Professor with the Department of Power Mechanical Engineering, National Tsing Hua University. His research interests include micromechanical resonator and oscillator design for wireless communication and signal processing, MEMS-ASIC integration technologies, and interface circuit design for MEMS-based microsystems.

Dr. Li received the Outstanding Engineering Student Scholarship from the Chinese Institute of Engineers in 2009 and the CTCI Foundation Science and Technology Research Scholarship in 2014. He also received the Best Student Paper Award from the 2011 Joint Conference of the IEEE International Frequency Control Symposium and the European Frequency and Time Forum (IFCS-EFTF 2011). He was a recipient of the Young Scholar Fellowship from the Ministry of Science and Technology, Taiwan, in 2019.

Songbin Gong (Senior Member, IEEE) received the Ph.D. degree in electrical engineering from the University of Virginia, Charlottesville, VA, USA, in 2010.

He is currently an Associate Professor and the Intel Alumni Fellow with the Department of Electrical and Computer Engineering and the Micro and Nanotechnology Laboratory, University of Illinois at Urbana–Champaign, Urbana, IL, USA. His research primarily focuses on design and implementation of radio frequency microsystems, components, and subsystems for reconfigurable RF front ends. In addition, his research explores hybrid microsystems based on the integration of MEMS devices with photonics or circuits for signal processing and sensing.

Dr. Gong is a Technical Committee Member of the MTT-21 RF-MEMS of the IEEE Microwave Theory and Techniques Society, the International Frequency Control Symposium, and the International Electron Devices Meeting. He was a recipient of the 2014 Defense Advanced Research Projects Agency Young Faculty Award, the 2017 NASA Early Career Faculty Award, the 2019 UIUC College of Engineer Dean's Award for Excellence in Research, and the 2019 Ultrasonics Early Career Investigator Award. Along with his students and postdoctorals, he received the Best Paper Awards from the 2017 and 2019 IEEE International Frequency Control Symposium and the 2018 and 2019 International Ultrasonics Symposium. He also received the Second Place in the Best Paper Competition from the 2018 IEEE International Microwave Symposium. He also serves as the Chair for MTT TC2 and TC 21. He serves as an Associate Editor for the IEEE TRANSACTIONS ON ULTRASONICS, FERROELECTRICS, AND FREQUENCY CONTROL (T-UFFC) and the *Journal of Microelectromechanical Systems* (JMEMS).